LETTER

doi:10.1038/nature22362

A cold-atom Fermi–Hubbard antiferromagnet

Anton Mazurenko[1], Christie S. Chiu[1], Geoffrey Ji[1], Maxwell F. Parsons[1], Márton Kanász-Nagy[1], Richard Schmidt[1], Fabian Grusdt[1], Eugene Demler[1], Daniel Greif[1] & Markus Greiner[1]

Exotic phenomena in systems with strongly correlated electrons emerge from the interplay between spin and motional degrees of freedom. For example, doping an antiferromagnet is expected to give rise to pseudogap states and high-temperature superconductors[1]. Quantum simulation[2–8] using ultracold fermions in optical lattices could help to answer open questions about the doped Hubbard Hamiltonian[9–14], and has recently been advanced by quantum gas microscopy[15–20]. Here we report the realization of an antiferromagnet in a repulsively interacting Fermi gas on a two-dimensional square lattice of about 80 sites at a temperature of 0.25 times the tunnelling energy. The antiferromagnetic long-range order manifests through the divergence of the correlation length, which reaches the size of the system, the development of a peak in the spin structure factor and a staggered magnetization that is close to the ground-state value. We hole-dope the system away from half-filling, towards a regime in which complex many-body states are expected, and find that strong magnetic correlations persist at the antiferromagnetic ordering vector up to dopings of about 15 per cent. In this regime, numerical simulations are challenging[21] and so experiments provide a valuable benchmark. Our results demonstrate that microscopy of cold atoms in optical lattices can help us to understand the low-temperature Fermi–Hubbard model.

The Hubbard Hamiltonian is a fundamental model for spin-1/2 lattice electrons and describes a competition between kinetic energy t and interaction energy U. In the limiting case of half-filling (an average of one particle per site) and dominant interactions ($U/t \gg 1$), the Hubbard model maps to the Heisenberg model. In this limit, the exchange energy $J = 4t^2/U$ gives rise to antiferromagnetically ordered states at low temperatures[22]. This order persists for all finite U/t, with charge fluctuations reducing the ordering strength. Away from half-filling, the coupling between motional and spin degrees of freedom is expected to lead to a complicated many-body phase diagram (Fig. 1a) that is challenging to understand theoretically owing to the fermion sign problem[21].

The strength of global antiferromagnetic order on bipartite lattices is quantified by the staggered magnetization $m = |\boldsymbol{m}|$. The component of this magnetization along the z spin direction is

$$m^z = \sqrt{\langle (\hat{m}^z)^2 \rangle} = \sqrt{\left\langle \left(\frac{1}{N} \sum_i (-1)^i \frac{\hat{S}_i^z}{S} \right)^2 \right\rangle} \qquad (1)$$

with $m^2 = (m^x)^2 + (m^y)^2 + (m^z)^2 = 3(m^z)^2$ for SU(2) symmetry[22]. Here $\hat{S}_i^z$ is a spin-S operator on lattice site i, N denotes the number of lattice sites, and $(-1)^i$ is 1 (−1) on the A (B) sublattice. The ground state of the classical Heisenberg model on a square lattice is a perfectly ordered Néel state with $m = 1$. However, in the quantum case, superposition states such as local singlet pairs can reduce the energy of the many-body state. These quantum corrections decrease the staggered magnetization in the ground state and in the thermodynamic limit to $m = 0.61$ ($m_z = 0.35$) for the $S = 1/2$ Heisenberg model[23]. In two dimensions, long-range order disappears ($m = 0$) in the thermodynamic limit for finite temperatures, in accordance with the Mermin–Wagner–Hohenberg theorem. In this case, the spin correlations decay exponentially over a correlation length ξ, which grows exponentially with inverse temperature (setting $k_B = 1$):

$$\xi(T) = C_\xi \exp\left(\frac{2\pi\rho_s}{T} \right) \qquad (2)$$

where ρ_s is the spin stiffness, T is the temperature and C_ξ is a constant[22]. However, for the finite-size system investigated here, a crossover to antiferromagnetic long-range order occurs at a non-zero temperature, at which ξ becomes comparable to the size of the system and m^z becomes order unity.

We created an antiferromagnet with long-range order governed by the Hubbard model using ultracold fermions in an optical lattice. Two aspects were critical for realizing the antiferromagnet: first, reaching sufficiently low temperatures; and second, creating a region of uniform density where a state with long-range order can form. We address both challenges simultaneously by exploiting a high-resolution microscope, which enables site-resolved measurements of the lattice occupation. In combination with the lattice, we finely tune the atomic potential landscape using a digital micromirror device in the image plane of the microscope as a spatial light modulator[24]. We engineer the potential to split the system into two subsystems: a central disk-shaped region Ω that contains more than 75 sites, and a large surrounding reservoir with much lower density (Fig. 1b, Extended Data Fig. 1). Partitioning the system enhances the inherent entropy redistribution in the trap by shifting a higher fraction of the total entropy to the reservoir[25]. Additionally, the potential within Ω is shaped to cancel out the underlying harmonic potential, ensuring a highly uniform and tunable filling (Extended Data Fig. 2, Methods).

We adiabatically load a balanced mixture of the two lowest hyperfine states of ^{6}Li with repulsive contact interactions into an isotropic, square, $7.4(1)E_R$ lattice with spacing $a = 569$ nm, where $E_R/h = 25.6$ kHz is the recoil energy, h is the Planck constant and all errors are defined as one standard deviation. The system is well described by the Hubbard model with $t/h = 0.90(2)$ kHz and $U/h = 6.50(3)$ kHz, which lead to $U/t = 7.2(2)$. Similarly to previous work, our detection method is based on selective spin removal followed by site-resolved imaging of the remaining atomic distribution[17] (Fig. 1c). Averaging over many independent experimental realizations, we determine the spin correlator along the z direction:

$$C_{\boldsymbol{d}} = \frac{1}{\mathcal{N}_{\boldsymbol{d}}} \frac{1}{S^2} \sum_{\substack{\boldsymbol{r},\boldsymbol{s}\in\Omega \\ \boldsymbol{d}=\boldsymbol{r}-\boldsymbol{s}}} \langle \hat{S}_{\boldsymbol{r}}^z \hat{S}_{\boldsymbol{s}}^z \rangle - \langle \hat{S}_{\boldsymbol{r}}^z \rangle \langle \hat{S}_{\boldsymbol{s}}^z \rangle$$

where the normalization $\mathcal{N}_{\boldsymbol{d}}$ is the number of different two-point correlators at displacement $\boldsymbol{d}$ between sites $\boldsymbol{r}$ and $\boldsymbol{s}$, which lie within Ω. The correlator compares the number of parallel and anti-parallel spin orientations on two sites separated by $\boldsymbol{d} = (d_x, d_y)$, and so is positive (negative) if parallel (anti-parallel) spin orientations are preferred. In Fig. 2a we show $C_{\boldsymbol{d}}$ for different temperatures. For the lowest temperature,

[1]Department of Physics, Harvard University, Cambridge, Massachusetts, USA.

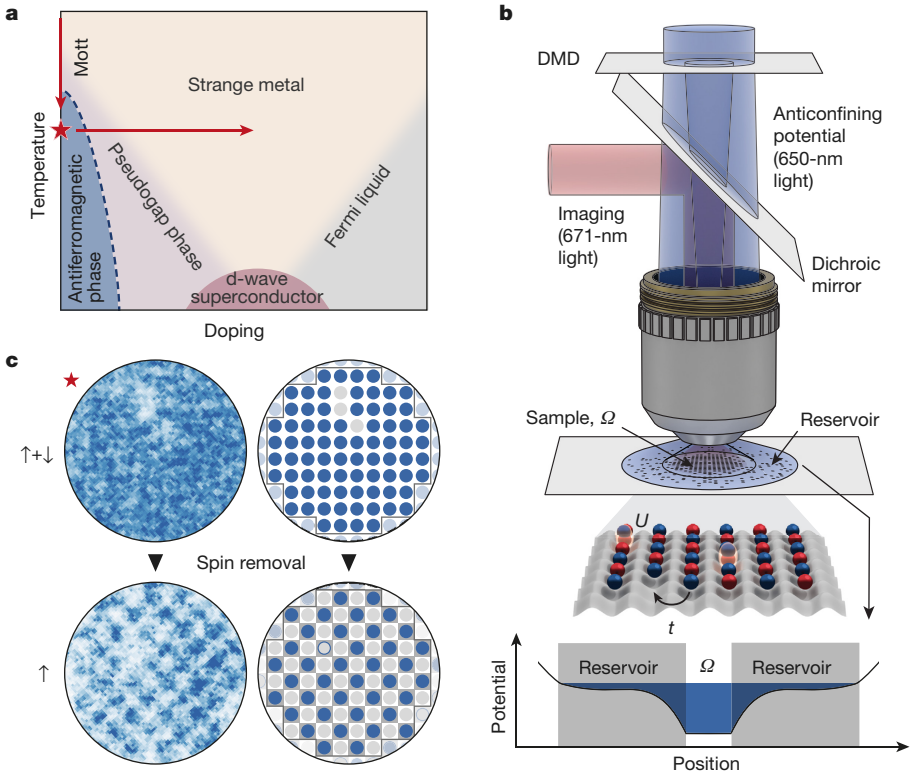

Figure 1 | Probing antiferromagnetism in the Hubbard model with a quantum gas microscope. a, Schematic of the two-dimensional Hubbard phase diagram, including predicted phases. We explore the trajectories traced by the red arrows for a Hubbard model with $U/t = 7.2(2)$. The strongest antiferromagnetic order is observed at the starred point. **b**, Experimental set-up. We trap ^{6}Li atoms in a two-dimensional square optical lattice. We use the combined potential of the optical lattice and the anticonfinement that is generated by the digital micromirror device (DMD) to trap the atoms in a central sample Ω of homogeneous density, surrounded by a dilute reservoir, as shown in the plot. The system is imaged with 671-nm light along the same beam path as the projected 650-nm potential, and separated from it by a dichroic mirror. **c**, Exemplary raw (left) and processed (right) images of the atomic distribution of single experimental realizations, with both spin components present (upper; corresponding to the starred point in **a**) and with one spin component removed (lower). The observed chequerboard pattern in the spin-removed images indicates the presence of an antiferromagnet.

we find spin correlations across the entire disk that alternate in sign even up to the largest distance of $d = |\boldsymbol{d}| = 10$, as expected for a state with antiferromagnetic long-range order. We determine the temperature of each sample by comparing the measured nearest-neighbour correlator C_1 to quantum Monte Carlo predictions at half-filling, which gives $T/t = 0.25(2)$ for the lowest temperature (Methods).

As temperature increases, the strength of antiferromagnetic order decreases rapidly, until for $T/t = 0.64(6)$ only nearest-neighbour spin correlations remain. To quantitatively analyse the spin correlations, we plot in Fig. 2b a binned azimuthal average of the sign-corrected spin correlator $(-1)^i C_{\boldsymbol{d}}$ as a function of distance d (Methods). For large distances ($d > 2$ sites), the measured correlation functions exhibit an exponential scaling with distance, verified by fitting $N_0 \exp(-d/\xi)$ to each dataset, with the correlation length ξ and N_0 as free parameters (but keeping N_0 the same across all fits). For our two-dimensional system, quantum fluctuations lead to an increase in spin correlations at short distances ($d \leq 2$) above the exponential dependence, most prominently visible in the nearest-neighbour correlator[26]. In Fig. 2d we show the experimentally determined correlation length as a function of temperature, which increases markedly at temperatures around $T/t = 0.4$. For the lowest temperature, we find a correlation length of $\xi = 8.3(9)$ sites, which is approximately equal to the system size of 10 sites, as expected for long-range order.

The long-wavelength and low-temperature behaviour of our system is expected to be well described by the quantum nonlinear σ model[27], which contains three fundamental ground-state parameters: the sublattice magnetization M, the spin stiffness constant ρ_s and the spin-wave velocity c. The spin stiffness quantifies the rigidity of an ordered spin system upon twisting, and has been calculated to be $\rho_s/t \approx 0.13$ for $U/t = 7$, slightly below the Heisenberg model value[28]. Because the temperatures and correlation lengths are independently determined in our experiment, we can obtain an experimental value of ρ_s directly by fitting the dependence in equation (2) to the data. The data show excellent agreement with the predicted exponential scaling of ξ with T^{-1} from equation (2). From the fit we determine $\rho_s/t = 0.16(1)$, which is larger than the calculated value, possibly owing to finite-size effects (Methods).

Antiferromagnetic long-range order in solid-state systems is typically detected by neutron scattering or magnetic X-ray scattering. These methods measure the spin structure factor at wavevector $\boldsymbol{q} = (q_x, q_y)$ and along the z direction, given by

$$S^z(\boldsymbol{q}) = \frac{1}{N} \sum_{\boldsymbol{r},\boldsymbol{s} \in \Omega}^{N} \frac{1}{S^2} \langle \hat{S}^z_{\boldsymbol{r}} \hat{S}^z_{\boldsymbol{s}} \rangle \exp\left[i\boldsymbol{q} \cdot (\boldsymbol{r} - \boldsymbol{s}) \right]$$

In a square lattice, antiferromagnetic long-range order manifests as a peak in the structure factor at $\boldsymbol{q}_{\mathrm{AFM}} = (\pi/a, \pi/a)$, the amplitude of which is directly related to the staggered magnetization: $m^z = \sqrt{S^z(\boldsymbol{q}_{\mathrm{AFM}})/N}$. For cold atom systems, the spin structure factor can be measured from noise correlations or Bragg scattering of light[14]. The site-resolved detection in our experiment enables a direct measurement of the spin structure factor, which is obtained from averaging the squared Fourier transformation of individual single-spin images (Methods). The same result is obtained when summing over all contributions of the spin correlation function (Extended Data Fig. 3).

For the lowest temperature, we observe a sharp peak in the structure factor at $\boldsymbol{q} = \boldsymbol{q}_{\mathrm{AFM}}$, which confirms the presence of antiferromagnetic long-range order (Fig. 2c). For increasing temperatures, the amplitude

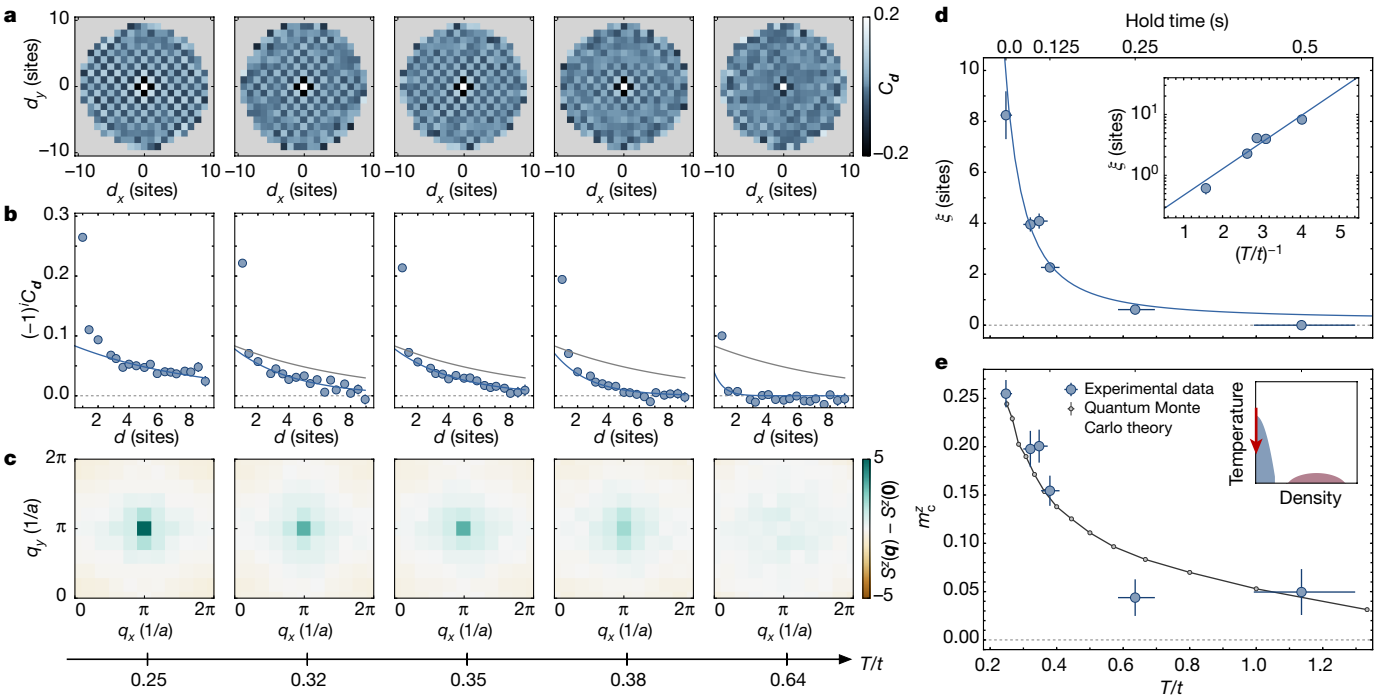

Figure 2 | Observing antiferromagnetic long-range order. a, The spin correlator $C_{\boldsymbol{d}}$ is plotted for different displacements $\boldsymbol{d} = (d_x, d_y)$ ranging across the entire sample for five temperatures T/t. We record more than 200 images for each temperature (Methods). Correlations extend across the entire sample for the coldest temperatures, whereas for the hottest temperature only nearest-neighbour correlations remain. **b**, The sign-corrected correlation function $(-1)^i C_{\boldsymbol{d}}$ is obtained through an azimuthal average. The exponential fits to the data ($|\boldsymbol{d}| = d > 2$ sites) are shown in blue, from which we determine the correlation length ξ; the fit of the coldest sample is plotted in grey in the other panels for comparison. **c**, The measured spin structure factor $S^z(\boldsymbol{q}) - S^z(\boldsymbol{0})$ obtained from Fourier transformations of single images. A peak at momentum $\boldsymbol{q}_{\mathrm{AFM}} = (\pi/a, \pi/a)$ signals the presence of an antiferromagnet. **d**, The measured correlation length ξ (data), fitted to equation (2) (curve), diverges exponentially as a function of temperature T/t and is comparable to the system size for the lowest temperature. The temperature is varied by holding the atoms in the trap for a variable time. The inset is a semi-logarithmic plot of the same quantity versus inverse temperature. **e**, The measured corrected staggered magnetization m_c^z (large blue circles) increases markedly below temperatures $T/t \approx 0.4$. We find good agreement with quantum Monte Carlo calculations of the Hubbard model (small grey circles). The trajectory followed in this figure is shown schematically in the phase diagram in the inset. Error bars in **d** and **e** are standard deviations of the sampled mean; error bars in **b** (smaller than the markers) are computed as in Methods. The figure is based on 2,282 experimental realizations.

of this peak decreases until it disappears for $T/t \gtrsim 0.64$, indicating the decay of long-range order. At these elevated temperatures, a broad peak with low amplitude remains, which originates from the remaining short-range spin correlations. We quantify the ordering strength of the antiferromagnetic long-range order by the corrected staggered magnetization $m_c^z(T)$, which subtracts uncorrelated contributions and is equal to m^z in the thermodynamic limit (Methods). Although initially small at elevated temperatures, m_c^z increases markedly at lower temperatures (Fig. 2d). We compare the measured temperature dependence to *ab initio* quantum Monte Carlo calculations of the Hubbard model on a 10 site × 10 site square lattice with periodic boundary conditions and no free parameters. We find agreement over the entire range of temperatures, with residual deviations possibly caused by the different spatial shape of Ω. The largest measured value of $m_c^z = 0.25(1)$ is more than 50% of the theoretically predicted zero-temperature value in the Heisenberg model for our system size, obtained from finite-size scaling[23].

The underlying Hubbard Hamiltonian that describes our system is SU(2)-symmetric. In the absence of a symmetry-breaking field, the staggered spin-ordering vector $\hat{\boldsymbol{m}} = (\hat{m}^x, \hat{m}^y, \hat{m}^z)$ is expected to point in random directions on a sphere between different experimental realizations. Consequently, individual measurements of the projection $\hat{m}^z$ are expected to have large variation. This variation is directly observable in our experiment, because we can measure independent values of the staggered magnetization operator $\hat{m}^z$ from single experimental realizations (Fig. 3a).

The variation of the staggered ordering can be quantified from a histogram of all measured values of $\hat{m}^z$ across different experimental realizations, which corresponds to the full counting statistics of the operator $\hat{m}^z$. These statistics are a powerful tool for characterizing many-body systems beyond average values[29], but so far have not been measured for the antiferromagnetic phase. In Fig. 3b we show the measured histograms of the staggered magnetization along the z direction for different temperatures at half-filling, each obtained from more than 250 images. All of the distributions are symmetric and peak around zero, with expectation values $\langle \hat{m}^z \rangle$ consistent with zero. In addition, we find the same results for spin correlations when measuring along a spin direction that is perpendicular to the z axis via a $\pi/2$ pulse (Extended Data Fig. 4). Both observations are consistent with a randomly oriented spin-ordering vector. The width of the distributions is characterized by the standard deviation m^z defined in equation (1). At the highest temperature, the distribution is consistent with the expectation in the infinite-temperature limit, in which the entire finite-size sample of N sites is uncorrelated. In this limit, a binomial distribution is predicted, with a width of $m^z(T \to \infty) = 1/\sqrt{N} = 0.1125$, which agrees with the experimentally measured value of $m^z = 0.12(2)$. At lower temperatures, the width of the distribution grows substantially and depends sensitively on temperature, but remains peaked around zero. The experimental data are in excellent agreement with *ab initio* quantum Monte Carlo calculations of the Heisenberg model at the experimentally determined temperatures. These findings show that the lattice thermometer based on nearest-neighbour correlations that we use here is correctly calibrated and very precise down to fractions of the tunnelling.

Whereas theoretical predictions at half-filling are available down to low temperature, this is not the case for doped systems, owing to the exponential scaling of the fermion sign problem with inverse

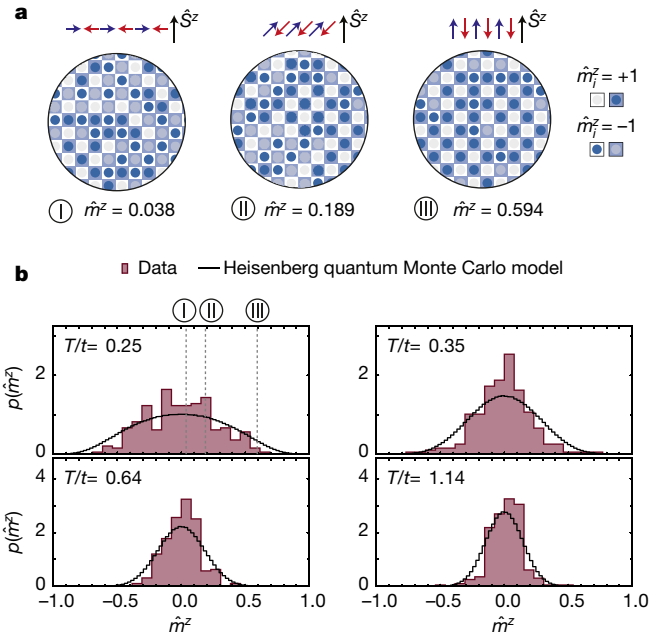

Figure 3 | Full counting statistics of the staggered magnetization operator. a, Selected images with one spin component removed (chequerboard overlaid to guide the eye) show a large variation in ordering strength at the coldest temperature. This variation is a consequence of the SU(2) symmetry of the underlying Hamiltonian, which leads to different orientations of the staggered spin-ordering vector $\hat{\boldsymbol{m}}$ relative to the measurement axis z, as shown schematically by the spin vectors (red and blue arrows) relative to the axis defined by $\hat{S}^z$ (black arrows). **b**, Measured distributions of the staggered magnetization operator, $p(\hat{m}_z)$, are plotted at different temperatures T/t (histograms). We find excellent agreement with quantum Monte Carlo simulations of the Heisenberg model with no free fitting parameters (black lines). The figure is based on 2,282 experimental realizations.

temperature, system size and interactions in this regime[21]. We can study the effect of doping on long-range order in our experiment directly by reducing the density of our sample and measuring the spin structure factor. Within the region Ω, we add a potential offset with the digital micromirror device for controlled hole doping, which is expected to also slightly change the temperature. We deduce the hole doping δ from the measured single-particle density n_s (Methods).

As shown in Fig. 4, the strongest magnetic correlations remain at $\boldsymbol{q} = \boldsymbol{q}_{\mathrm{AFM}}$. Doping gradually suppresses m_c^z, broadens the magnetic ordering peak in $S^z(\boldsymbol{q})$ and reduces its weight. Only at $\delta \gtrsim 0.15$ do we find that m_c^z settles to an approximately constant, small value. This offset originates from the strong short-range correlations that are still present at large dopings (Fig. 4b). When excluding the contributions of $d < 2$ from m_c^z, this offset disappears while the qualitative dependence $m_c^z(\delta)$ remains approximately the same (Extended Data Fig. 5). This finding suggests that for the finite-size, $U/t = 7.2$ Hubbard model studied here, strong magnetic correlations persist up to a critical hole doping $\delta_c \approx 0.15$. We note that our data might be consistent with incommensurate magnetism, which is commonly observed in high-temperature cuprate superconductors[30], because in our experiment finite-size effects and temperature broadening might prevent us from observing resolved peaks at wavevectors close to $\boldsymbol{q}_{\mathrm{AFM}}$.

We have realized a quantum antiferromagnet governed by the two-dimensional Hubbard Hamiltonian. Our architecture makes it possible to vary the doping and temperature, enabling us to explore the Hubbard phase diagram in theoretically challenging regimes. Attainable parameters are predicted to be sufficient to access the conjectured pseudogap[21] and stripe-ordered[1] phases. At lower temperatures $T/t \approx 0.05$ and dopings $\delta \approx 0.15$, theoretical work indicates a transition to a d-wave superconducting state[1]. Such temperatures could be achieved through advanced entropy redistribution schemes. Furthermore, entirely novel states of matter are within reach by augmenting the Hamiltonian with alternative lattice structures, artificial gauge fields and dipolar long-range interactions.

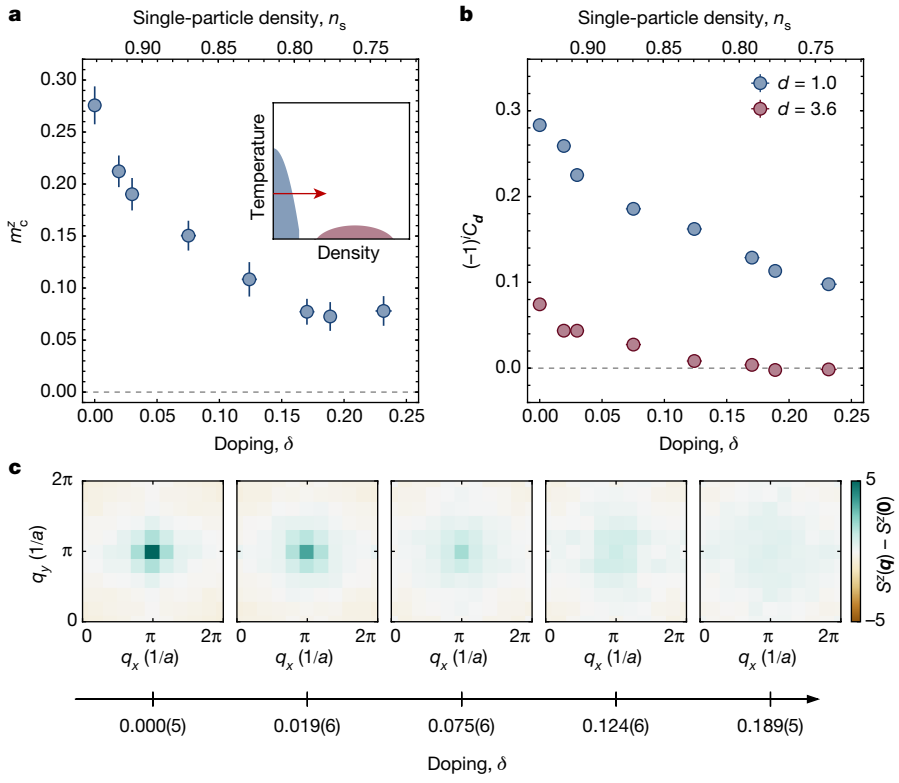

Figure 4 | Doping the antiferromagnet. a, We dope the system with holes and reduce the density from half-filling, with $0.0 \leq \delta \leq 0.25$ (corresponding to $0.95 \geq n_s \geq 0.73$). The corrected staggered magnetization m_c^z settles at the critical hole doping $\delta_c \approx 0.15$. The trajectory followed in this figure is shown schematically in the phase diagram in the inset. **b**, The relative strength of the sign-corrected spin correlations $(-1)^i C_d$ decreases less rapidly with hole doping at smaller distances ($d = 1.0$) than at larger distances ($d = 3.6$). For large doping, only the nearest-neighbour correlator is appreciable, so this correlation is predominantly responsible for the non-zero staggered magnetization away from the antiferromagnetic phase. **c**, We show the spin structure factor $S^z(\boldsymbol{q}) - S^z(\boldsymbol{0})$, as in Fig. 2c, for each doping value. Error bars in **a** are standard deviations of the sampled mean; those in **b** are computed as in Methods. The figure is based on 1,470 experimental realizations.

Online Content Methods, along with any additional Extended Data display items and Source Data, are available in the online version of the paper; references unique to these sections appear only in the online paper.

Received 16 December 2016; accepted 3 April 2017.

1. Lee, P., Nagaosa, N. & Wen, X.-G. Doping a Mott insulator: physics of high-temperature superconductivity. *Rev. Mod. Phys.* **78,** 17–85 (2006).
2. Friedenauer, A., Schmitz, H., Glueckert, J. T., Porras, D. & Schaetz, T. Simulating a quantum magnet with trapped ions. *Nat. Phys.* **4,** 757–761 (2008).
3. Kim, K. *et al.* Quantum simulation of frustrated Ising spins with trapped ions. *Nature* **465,** 590–593 (2010).
4. Struck, J. *et al.* Quantum simulation of frustrated classical magnetism in triangular optical lattices. *Science* **333,** 996–999 (2011).
5. Simon, J. *et al.* Quantum simulation of antiferromagnetic spin chains in an optical lattice. *Nature* **472,** 307–312 (2011).
6. Yan, B. *et al.* Observation of dipolar spin-exchange interactions with lattice-confined polar molecules. *Nature* **501,** 521–525 (2013).
7. Drewes, J. H. *et al.* Antiferromagnetic correlations in two-dimensional fermionic Mott-insulating and metallic phases. *Phys. Rev. Lett.* **118,** 170401 (2017).
8. Murmann, S. *et al.* Antiferromagnetic Heisenberg spin chain of a few cold atoms in a one-dimensional trap. *Phys. Rev. Lett.* **115,** 215301 (2015).
9. Hofstetter, W., Cirac, J. I., Zoller, P., Demler, E. & Lukin, M. D. High-temperature superfluidity of fermionic atoms in optical lattices. *Phys. Rev. Lett.* **89,** 220407 (2002).
10. Bloch, I., Dalibard, J. & Zwerger, W. Many-body physics with ultracold gases. *Rev. Mod. Phys.* **80,** 885–964 (2008).
11. Jördens, R., Strohmaier, N., Günter, K., Moritz, H. & Esslinger, T. A Mott insulator of fermionic atoms in an optical lattice. *Nature* **455,** 204–207 (2008).
12. Schneider, U. *et al.* Metallic and insulating phases of repulsively interacting fermions in a 3D optical lattice. *Science* **322,** 1520–1525 (2008).
13. Greif, D., Uehlinger, T., Jotzu, G., Tarruell, L. & Esslinger, T. Short-range quantum magnetism of ultracold fermions in an optical lattice. *Science* **340,** 1307–1310 (2013).
14. Hart, R. A. *et al.* Observation of antiferromagnetic correlations in the Hubbard model with ultracold atoms. *Nature* **519,** 211–214 (2015).
15. Haller, E. *et al.* Single-atom imaging of fermions in a quantum-gas microscope. *Nat. Phys.* **11,** 738–742 (2015).
16. Edge, G. J. A. *et al.* Imaging and addressing of individual fermionic atoms in an optical lattice. *Phys. Rev. A* **92,** 063406 (2015).
17. Parsons, M. F. *et al.* Site-resolved measurement of the spin-correlation function in the Fermi-Hubbard model. *Science* **353,** 1253–1256 (2016).
18. Boll, M. *et al.* Spin- and density-resolved microscopy of antiferromagnetic correlations in Fermi-Hubbard chains. *Science* **353,** 1257–1260 (2016).
19. Cheuk, L. W. *et al.* Observation of spatial charge and spin correlations in the 2D Fermi-Hubbard model. *Science* **353,** 1260–1264 (2016).
20. Brown, P. T. *et al.* Observation of canted antiferromagnetism with ultracold fermions in an optical lattice. Preprint at https://arxiv.org/abs/1612.07746 (2016).
21. Staar, P., Maier, T. & Schulthess, T. C. Dynamical cluster approximation with continuous lattice self energy. *Phys. Rev. B* **88,** 115101 (2013).
22. Manousakis, E. The spin-1/2 Heisenberg antiferromagnet on a square lattice and its application to the cuprous oxides. *Rev. Mod. Phys.* **63,** 1–62 (1991).
23. Sandvik, A. W. Finite-size scaling of the ground-state parameters of the two-dimensional Heisenberg model. *Phys. Rev. B* **56,** 11678–11690 (1997).
24. Liang, J., Kohn, R. N., Becker, M. F. & Heinzen, D. J. High-precision laser beam shaping using a binary-amplitude spatial light modulator. *Appl. Opt.* **49,** 1323–1330 (2010).
25. Ho, T.-L. & Zhou, Q. Universal cooling scheme for quantum simulation. Preprint at https://arxiv.org/abs/0911.5506 (2009).
26. Gorelik, E. V. *et al.* Universal probes for antiferromagnetic correlations and entropy in cold fermions on optical lattices. *Phys. Rev. A* **85,** 061602 (2012).
27. Chakravarty, S., Halperin, B. I. & Nelson, D. R. Two-dimensional quantum Heisenberg antiferromagnet at low temperatures. *Phys. Rev. B* **39,** 2344–2371 (1989).
28. Denteneer, P. J. H. & Van Leeuwen, J. M. J. Spin waves in the half-filled Hubbard Model beyond the random phase approximation. *Europhys. Lett.* **22,** 413–418 (1993).
29. Hofferberth, S. *et al.* Probing quantum and thermal noise in an interacting many-body system. *Nat. Phys.* **4,** 489–495 (2008).
30. Yamada, K. *et al.* Doping dependence of the spatially modulated dynamical spin correlations and the superconducting-transition temperature in $La_{2-x}Sr_xCuO_4$. *Phys. Rev. B* **57,** 6165–6172 (1998).

Acknowledgements We thank R. Desbuquois, S. Dickerson, A. Eberlein, A. Kaufman, M. Messer, N. Prokov'ev, S. Sachdev, R. Scalettar, B. Svistunov, W. Zwerger, and M. Zwierlein and his research group for discussions. We thank S. Blatt, D. Cotta, S. Fölling, F. Huber, W. Setiawan and K. Wooley-Brown for early-stage contributions to the experiment. We acknowledge support from AFOSR (MURI), ARO (MURI, NDSEG), the Gordon and Betty Moore foundation EPiQS initiative, HQOC, NSF (CUA, ITAMP, GRFP, SAO) and SNSF.

Author Contributions A.M., C.S.C., G.J., M.F.P. and D.G. performed the experiment and analysed the data. G.J. carried out the determinant quantum Monte Carlo calculations for Fig. 2e using the QUEST package. M.K.-N. developed the QMC code for the full-counting statistics and analysed the results together with R.S., F.G. and E.D. M.G. supervised the work. All authors contributed extensively to the writing of the manuscript and to discussions.

Author Information Reprints and permissions information is available at www.nature.com/reprints. The authors declare no competing financial interests. Readers are welcome to comment on the online version of the paper. Publisher's note: Springer Nature remains neutral with regard to jurisdictional claims in published maps and institutional affiliations. Correspondence and requests for materials should be addressed to M.G. (greiner@physics.harvard.edu).

Reviewer Information *Nature* thanks T. Giamarchi and the other anonymous reviewer(s) for their contribution to the peer review of this work.

METHODS

State preparation. The low-temperature Fermi gas is prepared using a sequence similar to previous work, whereby a balanced mixture of the two lowest hyperfine states of ^{6}Li with repulsive interactions is loaded into a 2D optical dipole trap[17]. Before loading the lattice from the dipole trap we ramp to the final magnetic bias field used in the experiment, 576 G, which corresponds to a scattering length of $210a_0$, where a_0 is the Bohr radius, and an interaction energy of $U/h = 6.50(3)$ kHz. This ramp includes a fast ramp over the narrow s-wave resonance at 543 G to avoid heating and loss. We then perform a final stage of evaporation immediately before loading the lattice, under a magnetic gradient. The magnetic gradient is then removed and we slowly load the atomic cloud within 40 ms into a square optical lattice with tunnelling $t_x/h = 9.1(1) \times 10^2$ Hz and $t_y/h = 9.0(1) \times 10^2$ Hz, with a lattice spacing of $a = 569$ nm. The illumination of the digital micromirror device (DMD) with blue-detuned light at wavelength $\lambda = 650$ nm is increased concurrently with the optical lattice. The populated layer lies at the focus of a high-resolution microscope system, which allows site-resolved detection of the lattice occupation and, at the same time, enables us to augment the harmonic lattice trap by projecting an approximately ring-shaped potential onto the atoms from a DMD in the image plane. The centre of the ring contains the correct potential to prepare the subsystem Ω, and the rim of the ring is shaped to reduce the filling of the reservoir[24].

To vary the temperature of the sample, the atomic gas is held in the combined lattice and 650-nm blue-detuned light potential for a variable time. The final evaporation set point is chosen such that the final state is at half-filling (that is, more atoms for higher temperatures). For the coldest temperature samples (zero hold time), approximately 400 atoms remain in the trap at a temperature $T \approx 0.1 T_F$, where T_F is the Fermi temperature. To vary the density of the sample, the level of the blue-detuned light field is adjusted with the DMD, as described in the next section.

Potential engineering. In addition to the underlying harmonic well that is generated by the optical lattice, an incoherent, blue-detuned ring-shaped light field partitions the system into a sparsely filled reservoir and densely filled central region Ω (Fig. 1). The blue detuned light has a wavelength of 650 nm with a bandwidth of 10 nm. The light is generated by an SLED (Exalos, EXS210044) amplified by two tapered amplifiers (Eagleyard, EYP-TPA-0650-00250-2007-CMT02-0000) in series.

The DMD is a flexible tool for projecting nearly arbitrary light fields on the atomic system[24,31–33]. The device is placed in the image plane of the system. This prevents direct access to the phase of the light field and makes it nearly impossible to produce single-site-sized features. However, the image plane approach is technically robust and suitable for applying weak potentials on larger length scales. Despite the close detuning of the light field, the low intensity ensures that the single-photon heating does not play a part on experimentally relevant timescales.

We use the TI Lightcrafter 6500 DMD evaluation board, which features a pixel resolution of 1,920 × 1,080 with 7.56 μm × 7.56 μm mirrors. During each experimental cycle, a pattern is loaded onto the DMD and the mirrors are fixed in place for the duration of the exposure. Because the DMD is a binary device, the desired pattern has to be converted into binary form using Floyd–Steinberg error diffusion.

The desired ring-shaped potential is a 2D piecewise-defined function that is optimized experimentally (Extended Data Fig. 1). The reservoir is created by a combination of a broad Gaussian peak that compensates the underlying harmonic confinement and a gradient term that compensates any residual potential gradients in the system. The central part that creates the Ω region is created by a depression in the light field and is curved to ensure that the total potential seen by atoms within Ω is flat. Variants of the DMD-engineered potential are shown in Extended Data Fig. 1, simulated by applying a Fourier optics-based transfer function to the input signal and accounting for the incident mode shape on the DMD. The flatness of the potential within Ω is critical to the realization of uniform antiferromagnetic long-range order because the hole doping is seen to strongly affect magnetic correlations. We characterize the flatness of the potential by measuring the atomic density distribution within Ω (Extended Data Fig. 2). Azimuthal averaging reveals that the resulting density is flat to within <4% over approximately 80 sites. To explore controlled doping levels, the absolute offset of the central potential is tuned by varying the depth of the central depression in the DMD pattern (Extended Data Fig. 1).

Detection methods. Details regarding the spin-removal process, site-resolved imaging and analysis of site-resolved images can be found in previous work[17,34]. Spin removal begins by rapidly reducing the tunnelling by increasing the lattice depth to $50E_R$. The lattice depth ramp occurs over 5 ms to maximize the single-particle density for the temperature dataset, whereas it occurs over 0.8 ms to reduce the doping fluctuations for a given doping set point for the doping dataset.

For each temperature value in the temperature dataset and for each doping value in the doping dataset, we take 70 images with no spin removed, 70 with one spin removed and 70 with the other spin removed.

Data analysis. All quantities presented here are extracted from a circular section of 10 lattice sites in diameter, denoted Ω. This disk is centred at the centre of mass of sites exceeding 80% filling, as measured from the images with no spin removal. Sites are included in Ω if the centre of the site is within the bounds of the circle. Because the centre of mass is a non-integer coordinate, our system sizes vary between 75 and 81 sites depending on the exact location of the centre within a lattice site. We find that, in all cases, the filling is constant across the disk. The entire region Ω is then used for all calculations of spin correlations, spin structure factor and staggered magnetization. We determine the temperature of each sample by comparing the largest measured nearest-neighbour correlator in Ω to quantum Monte Carlo predictions at half-filling[35].

We calculate the average site-resolved spin correlator for a given displacement C_d by averaging the correlator over all pairs of sites within Ω with the given displacement. We extract this quantity using the "alternative" method (C'_{alt}) method defined in ref. 17, because it has lower uncertainty for small values of C_d. Displacement vectors that have fewer than 100 total pairs of sites across all images are discarded. To calculate the spin correlation function versus distance, the displacements are split into bins of 0.3 sites, and averaged across them. Because of the non-integer centre of Ω, the largest distances may appear infrequently, so we discard bins for distances of larger than 5 sites if there are fewer than 5 contributions in that bin. Errors on the spin correlator are calculated as in previous work[17], and the errors on the spin correlation function are propagated using conventional techniques that assume that the spin correlation errors are normally distributed.

For the structure factor we first inscribe the circular section Ω into a minimal-size square (see Methods section 'Data analysis'). In the associated occupation matrix, atoms are denoted as 1, unoccupied sites denoted as −1 and sites introduced from placing the circular section in a square array denoted as 0. We compute the square of the magnitude of the Fourier transform of this array and average across all experimental realizations:

$$\langle |\mathcal{F}(\boldsymbol{q})|^2 \rangle = \left\langle \sum_{\boldsymbol{r},\boldsymbol{s}} e^{i\boldsymbol{q}\cdot(\boldsymbol{r}-\boldsymbol{s})} [\hat{S}^z_{\boldsymbol{r}} + (\hat{m}^z_{0,\boldsymbol{r}})^2 - 1][\hat{S}^z_{\boldsymbol{s}} + (\hat{m}^z_{0,\boldsymbol{s}})^2 - 1] \right\rangle$$
$$= NS^z(\boldsymbol{q}) + \left| \sum_{\boldsymbol{r}} e^{i\boldsymbol{q}\cdot\boldsymbol{r}} \langle (\hat{m}^z_{0,\boldsymbol{r}})^2 - 1 \rangle \right|^2$$

which implies

$$S^z(\boldsymbol{q}) = \frac{1}{N}\left[\langle |\mathcal{F}(\boldsymbol{q})|^2 \rangle - \left| \sum_{\boldsymbol{r}} e^{i\boldsymbol{q}\cdot\boldsymbol{r}} \langle 1 - (m^z_{0,\boldsymbol{r}})^2 \rangle \right|^2 \right]$$

where N is the number of sites, $S^z(\boldsymbol{q})$ is the spin structure factor, $\hat{S}^z_{\boldsymbol{r}}$ is the spin operator at site $\boldsymbol{r}$, $(\hat{m}^z_{0,\boldsymbol{r}})^2$ is the local moment operator and, owing to spin balance, $\langle \hat{S}^z_{\boldsymbol{r}}[(\hat{m}^z_{0,\boldsymbol{s}})^2 - 1] \rangle = 0$. Errors are calculated by assuming that the distribution of $S^z(\boldsymbol{q})$ is normal. Although there are finite bounds on the possible values of the spin structure factor, the histograms in Fig. 3 demonstrate that the assumption of normality is reasonable.

In the thermodynamic limit, the root-mean-square staggered magnetization is

$$m^z = \sqrt{\frac{1}{N} S(\boldsymbol{q} = (\pi/a, \pi/a))}$$

For finite systems this expression is non-zero even in the paramagnetic limit. We remove the finite offset and normalize such that the minimum value is 0 in the absence of spin correlations and the maximum value is 1:

$$m^z_{\mathrm{c}} = \sqrt{|S^z(\boldsymbol{q}_{\mathrm{AFM}}) - S^z(\boldsymbol{0})|} \sqrt{\frac{N}{N^2 - N}}$$

Errors are propagated from the computed spin structure factor using standard techniques. We verify that the value that results from the Fourier-based computation agrees with the value obtained by summing individual site-resolved spin correlations, which explicitly accounts for doublons and holes in the sample (Extended Data Fig. 3; owing to spin balance, $\langle S^z_{\boldsymbol{r}} \rangle = 0$).

System calibrations. The system is calibrated using parametric lattice modulation spectroscopy, whereby the lattice is modulated at varied frequencies. When the modulation frequency matches an inter-band transition, substantial loss of atoms is seen. The inter-band transition frequencies are fitted to a Mathieu equation model, and a conversion between lattice laser power and lattice depth is extracted, which sets the tunnelling parameter t. The interaction strength U is estimated from the scattering length at the applied magnetic field and the lattice depths along the x, y and z directions.

Theoretical methods. In the region Ω, our system is well described by the single-band, homogeneous, two-component Hubbard model on a square lattice[36]:

$$\hat{H} = -t \sum_{\sigma,\langle i,j\rangle \in \Omega} (\hat{c}^{\dagger}_{i,\sigma}\hat{c}_{j,\sigma} + \text{h.c.}) + U \sum_{i\in\Omega} \hat{n}_{i,\downarrow}\hat{n}_{i,\uparrow}$$

where $\langle i,j\rangle$ are nearest-neighbours, $\hat{c}_{i,\sigma}$ and $\hat{n}_{i,\sigma} = \hat{c}^{\dagger}_{i,\sigma}\hat{c}_{i,\sigma}$ are the annihilation and number operator of spin $\sigma \in \{\uparrow, \downarrow\}$ on site i, respectively, and 'h.c.' is the Hermitian conjugate. The on-site spin operators are defined as $\hat{S}^{\alpha}_{i} = \hat{c}^{\dagger}_{i,\beta}\sigma^{\alpha}_{\beta\gamma}\hat{c}_{i,\gamma}/2$ where σ^{α} are the Pauli spin matrices.

Close to half-filling and at temperatures well below the interaction energy, the Hubbard model exhibits a linear relationship between a change in the single-particle occupation δ_{single} and doping of the total density δ. Using numerical data obtained from the dynamical cluster approximation[37,38] method at $U/t = 7.2$ and $T/t = 0.25$, we obtain a fitted slope of $\delta = 1.22(1) \times \delta_{\text{single}}$. The relationship we obtain is consistent with results obtained from a re-summed numerical linked-cluster expansion[39] (NLCE) method for dopings of less than 6%, above which the re-summed NLCE data become unstable. We use this result to calculate the hole doping given the single-particle doping in Fig. 4. When the system is hole-doped, potential incommensurate order has been conjectured to occur[40,41].

The quantum nonlinear σ model mentioned in the main text was originally introduced to describe the low-temperature Heisenberg model[27,42,43]. Finite-size effects are expected to increase the spin stiffness ρ_s (ref. 44).

For the theoretical prediction in Fig. 2d, we performed determinant quantum Monte Carlo on the 10×10 2D Hubbard model with periodic boundary conditions and $U/t = 7.2$ using the QUEST package[45–47]. At low temperatures, the system does not sample different orientations of the staggered magnetization isotropically within the 10^4 measurement sweeps, so the reported magnetization is averaged over 14 independent runs and averaged over all three axes.

Histograms. Full counting statistics (FCS) are a powerful tool for characterizing quantum states and phenomena in various systems[48–51]. For example, they have been used to observe the quantization of electrical charge in shot-noise measurements[52] and the fractional charges in fractional quantum Hall systems[53–55], and to characterize prethermalization in an ultracold atomic set-up[29,56,57]. Here we determine the FCS of the staggered magnetization operator $\hat{m}^z = (1/N)\sum_i (-1)^i S^z_i/S$ from an *ab initio* quantum Monte Carlo simulation of the antiferromagnetic Heisenberg model[58,59]

$$\hat{H} = J \sum_{\langle i,j\rangle} \hat{\mathbf{S}}_i \cdot \hat{\mathbf{S}}_j$$

To this end, we implement a stochastic series-expansion quantum Monte Carlo calculation with operator loop updates[60]. We simulate a 16×16 system with periodic boundary conditions, and calculate the FCS of $\hat{m}^z$ in a smaller 9×9 region, which is of similar size to the measurement region used in the experiment. In our model, the spins outside of the measurement area serve as an effective thermal bath, mimicking the experimental set-up. The presence of the bath introduces additional fluctuations compared to a system of equal size but with periodic boundary conditions, leading to further suppression of large values of the staggered magnetization at the lowest temperatures in Fig. 3.

As shown in Fig. 3, the distribution of the measured values of $\hat{m}^z$ shows qualitatively different characteristics at high and low temperatures, which are imposed by the infinite- and zero-temperature limits. In the infinite-temperature limit, the spins take on uncorrelated random values. In the limit of vanishing temperatures and large system sizes, we expect the distribution to be flat up to a maximum value given by the length of the quantum mechanical spin-ordering vector $\boldsymbol{m}$, which reflects the simple model in which the vector pointing in random directions on a sphere has a fixed length. In a system of N measured sites, the FCS therefore have the same distribution as N independent coin flips, which approaches a binomial distribution of width $1/\sqrt{N}$ for large system sizes.

Alternative basis measurements. All measurements presented here were carried out in the $\hat{S}^z$ basis. SU(2) symmetry implies that correlations should exist along every possible measurement axis. To verify this, we added a $\pi/2$ pulse before the selective spin-removal pulse and measured correlations as before. Extended Data Fig. 4 shows that the correlations at all length scales are insensitive to the applied microwave field, regardless of whether no pulse, a $\pi/2$ pulse or a π pulse is performed. This outcome is consistent with the underlying state being SU(2)-symmetric, but is not sufficient to claim that it is so.

Data availability. The datasets generated and analysed during this study are available from the corresponding author on reasonable request.

31. Zupancic, P. *et al.* Ultra-precise holographic beam shaping for microscopic quantum control. *Opt. Express* **24,** 13881–13893 (2016).
32. Gaunt, A. L. *et al.* Robust digital holography for ultracold atom trapping. *Sci. Rep.* **2,** 721 (2012).
33. Hueck, K., Mazurenko, A., Luick, N., Lompe, T. & Moritz, H. Suppression of kHz-frequency switching noise in digital micro-mirror devices. *Rev. Sci. Instrum.* **88,** 016103 (2017).
34. Parsons, M. F. *et al.* Site-resolved imaging of fermionic ^{6}Li in an optical lattice. *Phys. Rev. Lett.* **114,** 213002 (2015).
35. Paiva, T., Scalettar, R., Randeria, M. & Trivedi, N. Fermions in 2D optical lattices: temperature and entropy scales for observing antiferromagnetism and superfluidity. *Phys. Rev. Lett.* **104,** 066406 (2010).
36. Hubbard, J. Electron correlations in narrow energy bands. *Proc. R. Soc. Lond. A* **276,** 238–257 (1963).
37. LeBlanc, J. P. F. & Gull, E. Equation of state of the fermionic two-dimensional Hubbard model. *Phys. Rev. B* **88,** 155108 (2013).
38. LeBlanc, J. P. F. *et al.* Solutions of the two-dimensional Hubbard model: benchmarks and results from a wide range of numerical algorithms. *Phys. Rev. X* **5,** 041041 (2015).
39. Khatami, E. & Rigol, M. Thermodynamics of strongly interacting fermions in two-dimensional optical lattices. *Phys. Rev. A* **84,** 053611 (2011).
40. Machida, K. Magnetism in La_2CuO_4 based compounds. *Physica C* **158,** 192–196 (1989).
41. Schulz, H. J. Incommensurate antiferromagnetism in the two-dimensional Hubbard model. *Phys. Rev. Lett.* **64,** 1445–1448 (1990).
42. Schulz, H. J. in *The Hubbard Model: Its Physics and Mathematical Physics* (eds Baeriswyl, D. *et al.*) 89–102 (Springer, 1995).
43. Chubukov, A. V., Sachdev, S. & Ye, J. Theory of two-dimensional quantum Heisenberg antiferromagnets with a nearly critical ground state. *Phys. Rev. B* **49,** 11919–11961 (1994).
44. Caffarel, M. *et al.* Monte Carlo calculation of the spin stiffness of the two-dimensional Heisenberg model. *Europhys. Lett.* **26,** 493–498 (1994).
45. Chang, C.-C., Gogolenko, S., Perez, J., Bai, Z. & Scalettar, R. T. Recent advances in determinant quantum Monte Carlo. *Phil. Mag.* **95,** 1260–1281 (2015).
46. Gogolenko, S., Bai, Z. & Scalettar, R. Structured orthogonal inversion of block p-cyclic matrices on multicores with GPU accelerators. In *Euro-Par 2014 Parallel Processing* (eds Silva, F. *et al.*) 524–535 (*Lecture Notes in Computer Science* Vol. 8632, Springer, 2014).
47. Jiang, C., Bai, Z. & Scalettar, R. T. A fast selected inversion algorithm for Green's function calculations in many-body quantum Monte Carlo simulations. In *Proc. 30th IEEE International Parallel and Distributed Processing Symposium* https://doi.org/10.1109/IPDPS.2016.69 (IEEE, 2016).
48. Cherng, R. W. & Demler, E. Quantum noise analysis of spin systems realized with cold atoms. *New J. Phys.* **9,** 7 (2007).
49. Braungardt, S., Sen(De), A., Sen, U., Glauber, R. J. & Lewenstein, M. Fermion and spin counting in strongly correlated systems. *Phys. Rev. A* **78,** 063613 (2008).
50. Braungardt, S. *et al.* Counting of fermions and spins in strongly correlated systems in and out of thermal equilibrium. *Phys. Rev. A* **83,** 013601 (2011).
51. Lamacraft, A. Noise and counting statistics of insulating phases in one-dimensional optical lattices. *Phys. Rev. A* **76,** 011603 (2007).
52. Blanter, Y. & Büttiker, M. Shot noise in mesoscopic conductors. *Phys. Rep.* **336,** 1–166 (2000).
53. de-Picciotto, R. *et al.* Direct observation of a fractional charge. *Nature* **389,** 162–164 (1997).
54. Saminadayar, L., Glattli, D. C., Jin, Y. & Etienne, B. Observation of the *e*/3 fractionally charged Laughlin quasiparticle. *Phys. Rev. Lett.* **79,** 2526–2529 (1997).
55. Goldman, V. J. & Su, B. Resonant tunneling in the quantum Hall regime: measurement of fractional charge. *Science* **267,** 1010–1012 (1995).
56. Gritsev, V., Altman, E., Demler, E. & Polkovnikov, A. Full quantum distribution of contrast in interference experiments between interacting one-dimensional Bose liquids. *Nat. Phys.* **2,** 705–709 (2006).
57. Polkovnikov, A., Altman, E. & Demler, E. Interference between independent fluctuating condensates. *Proc. Natl Acad. Sci. USA* **103,** 6125–6129 (2006).
58. Mermin, N. D. & Wagner, H. Absence of ferromagnetism or antiferromagnetism in one- or two-dimensional isotropic Heisenberg models. *Phys. Rev. Lett.* **17,** 1133–1136 (1966).
59. Hohenberg, P. C. Existence of long-range order in one and two dimensions. *Phys. Rev.* **158,** 383–386 (1967).
60. Sandvik, A. W. Stochastic series expansion method with operator-loop update. *Phys. Rev. B* **59,** R14157(R) (1999).

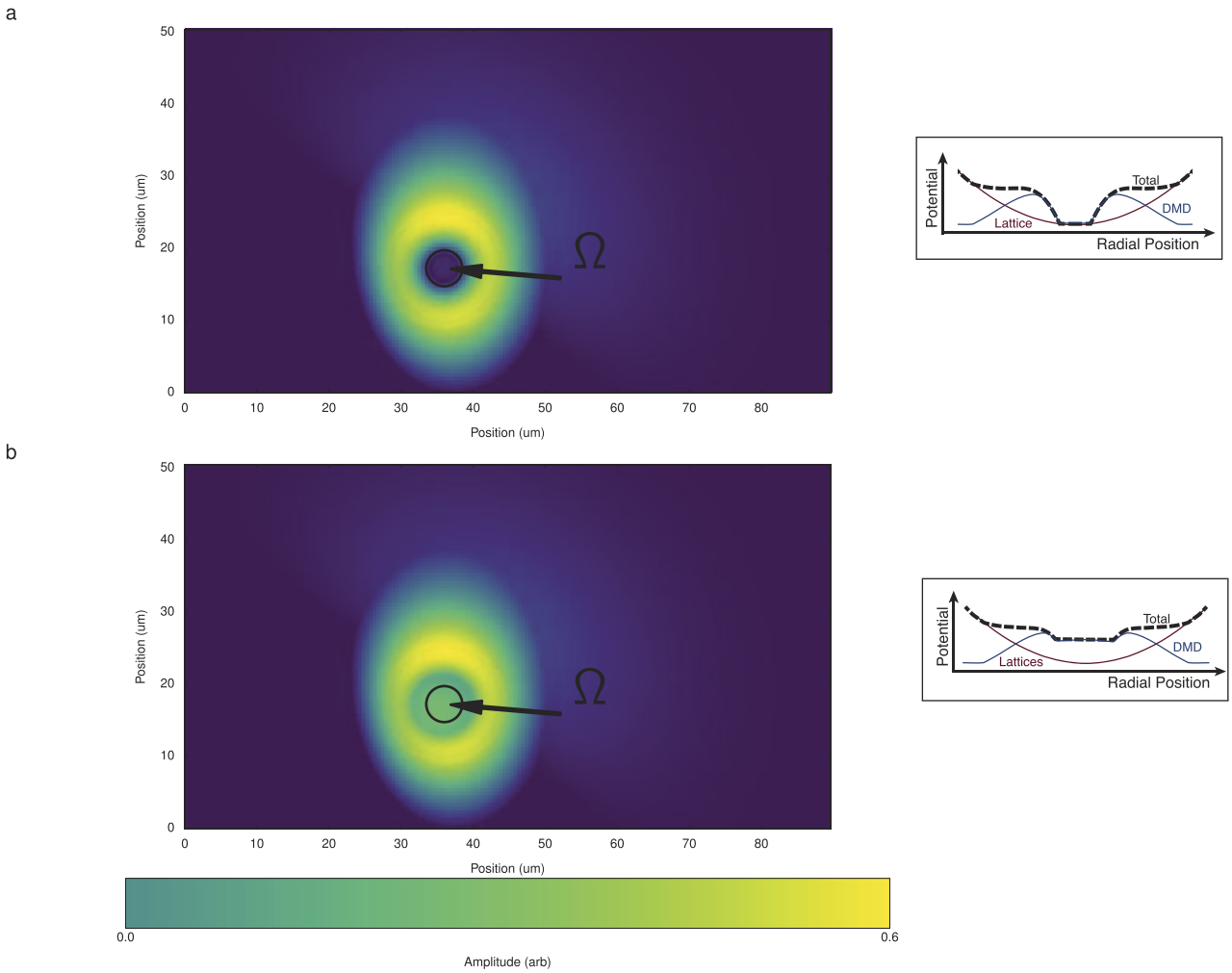

Extended Data Figure 1 | Amplitude of light fields applied to atoms. **a**, The computed light field generated by the DMD, applied to the atoms for half-filled samples. A gradient compensates residual gradients in the lattice. The rim of the doughnut provides sharp walls for the inner subsystem. A small peak in the centre flattens the potential when combined with the optical lattice. The plot on the right shows a schematic of a radial cut of the potential, including the contribution of the lattice. **b**, The amplitude of the light field with an offset in the centre of the trap, used to dope the system with a finite population of holes.

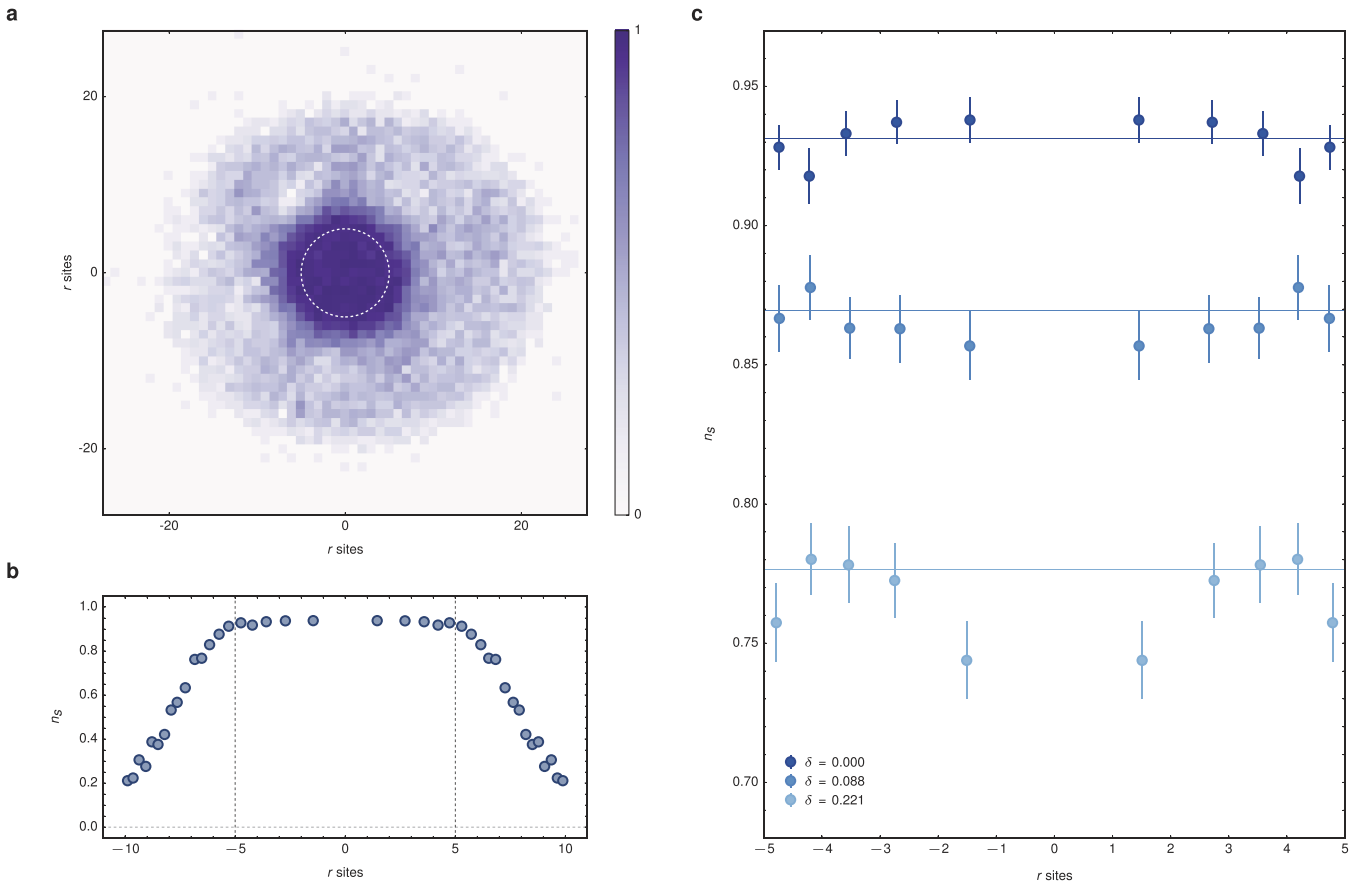

Extended Data Figure 2 | Average density profile in the system. a, The average single-particle density map for a sample at half-filling shows a central region of uniform density, surrounded by a doughnut-shaped ring of low density. The dotted white circle indicates our system size, excluding edge effects. **b**, The azimuthal average of the single-particle density n_s shown in **a**, for the system and for the inner edge of the doughnut where the density drops off to the reservoir density. The vertical dotted lines denote the boundary of the system. **c**, Azimuthal average of the single-particle density n_s for three values of the hole doping δ used in the experiment, indicating uniformity of atom number across our system to within 4%. The horizontal lines are at the system-wide average densities. Error bars in **c** are one standard deviation of the sample mean. The figure is based on 2,105 experimental realizations.

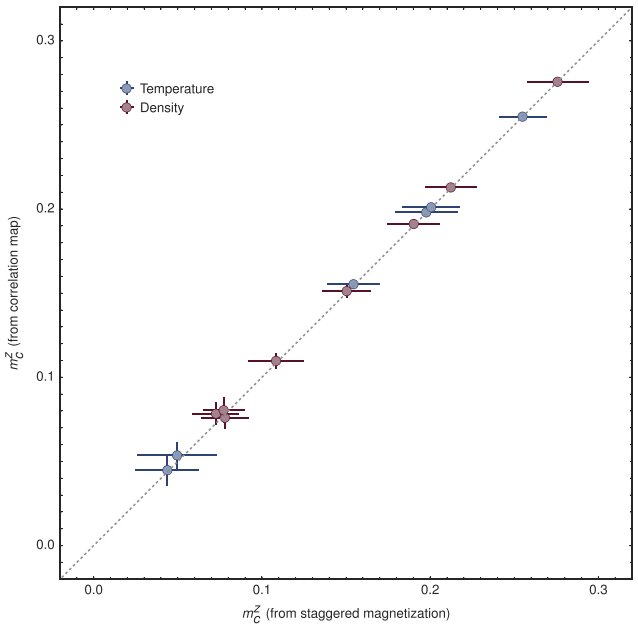

Extended Data Figure 3 | Comparison of staggered magnetizations obtained directly through single-spin images and from spin correlations. We calculate the corrected staggered magnetization m_c^z from images with one spin state removed (main text). It can also be calculated from the spin correlator (Methods), with the two methods being identical in the limit of no noise and exactly one particle per site. Plotting these two quantities against each other, we find very good agreement with the line $y = x$ (dotted line), indicating that any error due to deviation from one particle per site is small. The comparison is performed for the datasets used in Fig. 2 (labelled temperature) and Fig. 4 (labelled density). Error bars are computed as described in Methods.

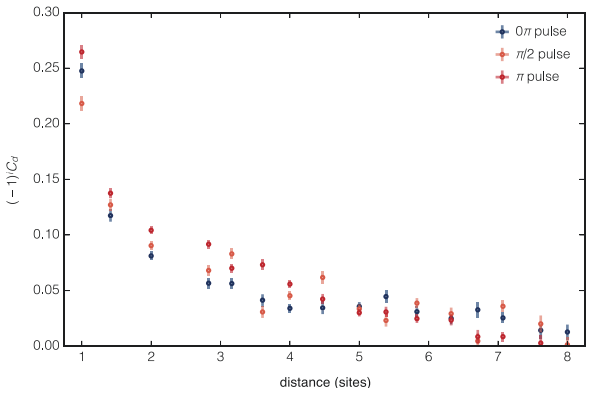

Extended Data Figure 4 | Alternative basis measurement. We optionally apply a π/2 or π microwave pulse before the spin removal pulse and correlation measurement. The sign-corrected spin correlation functions $(-1)^i C_d$ are insensitive to the presence and duration of this microwave pulse, consistent with an SU(2) symmetry of the state. The error bars are computed as described in Methods. This figure is based on 667 experimental realizations.

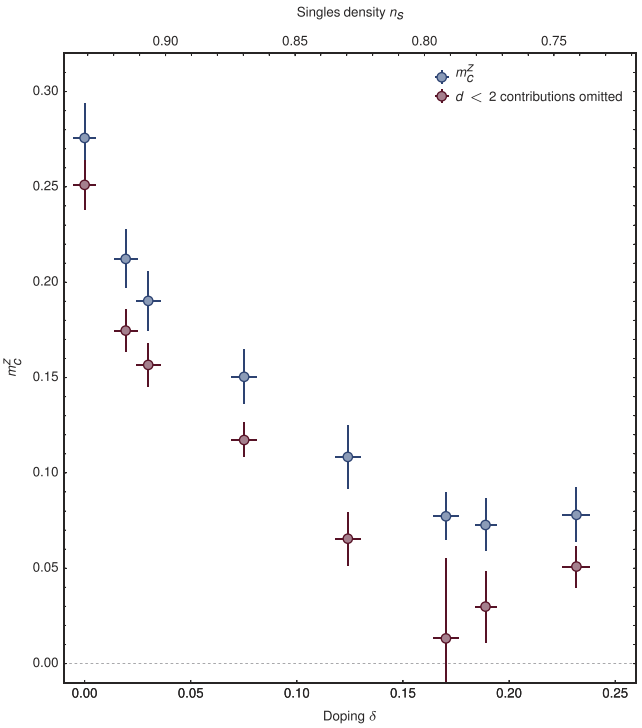

Extended Data Figure 5 | Staggered magnetization obtained from spin correlations, with and without the nearest-neighbour contribution included. To investigate the contributions to the corrected staggered magnetization m_c^z at high dopings δ, we consider the value calculated from the spin correlator (blue circles). We then omit the longest-range correlations, which have the greatest level of noise owing to the low number of pairs of sites extending across the cloud, as well as the nearest-neighbour correlations, which are essentially the only non-zero correlator outside of the antiferromagnetic phase (red circles). In the high-doping regime, we see that the greatest contribution to the staggered magnetization is the nearest-neighbour correlation, followed by the noisy longest-range correlations. Error bars are one standard deviation of the sample mean.